Investigation of Turbulent Mixing in a Confined Planar-Jet Reactor

Hua Feng and Michael G. Olsen
Dept. of Mechanical Engineering, Iowa State University, Ames, IA 50011

Ying Liu, Rodney O. Fox, and James C. Hill
Dept. of Chemical Engineering, Iowa State University, Ames, IA 50011

DOI 10.1002/aic.10527
Published online July 13, 2005 in Wiley InterScience (www.interscience.wiley.com).

The velocity and concentration fields in a liquid-phase confined planar-jet reactor were measured using particle image velocimetry (PIV) and planar laser-induced fluorescence (PLIF). Measurements were taken at downstream distances from the jet splitter plates of 0, 1, 4.5, 7.5, 12, and 15 jet widths for a Reynolds number of 50,000 based on the hydraulic diameter of the test section. The velocity and concentration field data were analyzed for such flow statistics as mean velocity, Reynolds stresses, turbulent kinetic energy, and scalar mean and variance. The turbulence dissipation rate was also estimated based on a large-eddy PIV approach using the strain-rate tensors computed from velocity fields and the subgrid scale (SGS) stress obtained from the Smagorinsky model. Computational fluid dynamics (CFD) models, including a two-layer k–ε turbulence model, gradient-diffusion models, and a scalar dissipation rate model, were validated against experimental data collected from this facility. The experimental and computational results were found to be in good agreement. © 2005 American Institute of Chemical Engineers
AIChE J, 51: 2649–2664, 2005
Keywords: PIV, PLIF, turbulent mixing, planar jet, computational fluid dynamics

Introduction

Because of their ability to transport and mix chemical species, momentum, and energy much faster than by molecular diffusion alone, turbulent flows are widely used in the chemical process industry. For example, most chemical reactors are designed to operate in the turbulent regime to maximize throughput. It follows that a detailed understanding of turbulent mixing is necessary for the proper design and optimization of chemical reactors, making turbulent mixing the topic of numerous experimental and computational studies over the years.[1-4] One objective in studying turbulent mixing is to develop computational fluid dynamics (CFD) models for turbulent reacting flows.[5] Because of its potential for quickly generating flow-field predictions in complex geometries at a relatively low cost, CFD can be a useful tool in reactor design and analysis.[6] One key component of a successful CFD model is the model used to characterize turbulent mixing at the microscale.[5,7-9] Both the development and validation of subgrid-scale (SGS) models require comparison with experimental data.[10,11] Accordingly, experimental studies can be of great importance in both advancing turbulence theory and in the development and validation of CFD micromixing models. The primary objective of this work is to implement state-of-the-art experimental techniques to validate CFD models for turbulent mixing in a well-defined flow geometry: a confined planar-jet reactor.

In the present study, velocity and concentration fields in a turbulent flow have been measured using two nonintrusive optically based techniques: particle image velocimetry (PIV)

Correspondence concerning this article should be addressed to M. G. Olsen at mgolsen@iastate.edu.

and planar laser-induced fluorescence (PLIF). After their rapid development in recent years, both PIV and PLIF have been proven to be capable of providing high-quality measurements. Aanen et al.[12] tested the reliability and precision of the techniques of PIV and PLIF. They measured the mixing of fluorescein emitted from a point source placed in the center of a fully developed turbulent flow in a smooth pipe and found that the experimental results agreed well with those of a direct numerical simulation (DNS) and the analytical results. In their paper on the mixing in a self-preserving axisymmetric turbulent jet, Fukushima et al.[13] compared their results obtained from PIV and PLIF techniques with not only the results from DNS, but also with point velocity measurements and combined PIV, particle-tracking velocimetry (PTV), or laser Doppler velocimetry (LDV) with laser-induced fluorescence (LIF) measurements, and found satisfactory agreement between the DNS simulations and the data collected using each technique. Meyer et al.[14] also measured the velocity field and concentration field using PIV and PLIF. They considered the mixing of a jet in a crossflow in a square duct and compared their results with measurements in the same setup by the use of pointwise LIF and laser Doppler anemometry (LDA). They found that PIV and PLIF gave results in good agreement with those from single-point techniques. Furthermore, as whole-field measurement techniques, both PIV and PLIF have distinct advantages over single-point measurement techniques, especially in their ability to give instantaneous spatial information. For this reason, PIV and PLIF have been used to investigate the spatial structure of turbulent velocity and concentration fields.[15-17]

In collecting experimental data to develop or validate computational models, one would like to perform experiments with enough spatial resolution to accurately determine flow quantities such as Reynolds stresses and dissipation rates. According to classical turbulence theory,[18] the characteristic scale of the smallest turbulent motions is the Kolmogorov scale, which is defined by

$$\eta = \left(\frac{\nu^3}{\varepsilon}\right)^{1/4} \tag{1}$$

where ν is the molecular kinematic viscosity and ε is the rate of dissipation of turbulent kinetic energy per unit mass.

Mixing layer growth and fluid entrainment are dominated by large-scale turbulent structures.[19-21] Large-scale structures absorb energy from the mean flow and are usually flow dependent, whereas small-scale structures mainly dissipate the energy provided by larger eddies and are more universal than the large scales.[22] For high Reynolds number flows, only the large-scale turbulent structures need to be resolved to determine the Reynolds stresses and turbulent kinetic energy because they are the energy-containing structures. For example, Law and Wang[23] studied turbulent mixing using PIV with a spatial resolution of about 16η and obtained turbulence intensities in good agreement with results from fine-scale measurements. Smaller scales must be resolved if one desires to measure or estimate turbulence dissipation. Tennekes and Lumley[24] suggested that the spatial resolution of the velocity measurement be no more than 5η, where the dissipation of the turbulence has a maximum. Tsurikov and Clemens[25] found that kinetic energy–dissipative structures have thicknesses ranging from approximately 1η to 10η and a mean thickness of 4η after processing the PIV data at a few different resolutions.

In homogeneous and isotropic turbulence, the mean turbulence dissipation rate ε can be approximated by

$$\varepsilon \approx A\,\frac{u_0'^3}{l} \tag{2}$$

where u_0' is the characteristic fluctuating velocity, l represents the integral length scale of turbulence, and A is a constant.[24,26] Antonia et al.[27] found that the value of $A \cong 1$ if Eq. 2 is applied to planar jets. In practice, the integral length scale is not a constant and varies throughout the flow field, so that Eq. 2 cannot be used to calculate the local dissipation rate. Numerous methods have been suggested to estimate the local dissipation rate from hot wire or laser Doppler anemometry data.[28,29] However, these methods are limited because of their being single-point velocity techniques. Because of the planar nature of the collected data, PIV offers the possibility of estimating the distribution of the dissipation rate over a large flow region. Based on a large-eddy PIV approach, Sheng et al.[30] showed that the turbulence dissipation rate could be approximated by computing the Reynolds averaged SGS dissipation rate

$$\varepsilon \approx -2\langle \tau_{ij}\bar{S}_{ij}\rangle \tag{3}$$

where $\bar{S}_{ij}$ is the filtered rate-of-strain tensor defined by

$$\bar{S}_{ij} = \frac{1}{2}\left(\frac{\partial \bar{U}_j}{\partial x_i} + \frac{\partial \bar{U}_i}{\partial x_j}\right) \tag{4}$$

where $\bar{U}$ is the filtered velocity field. To close the SGS stress τ_{ij}, various SGS models have been proposed. The Smagorinsky model[31] is one of the simplest models, which gives

$$\tau_{ij} = -C_S^2\Delta^2|\bar{S}|\bar{S}_{ij} \tag{5}$$

where $C_s = 0.17$ is the Smagorinsky constant, Δ is the filter width, and $|\bar{S}| = (2\bar{S}_{ij}\bar{S}_{ij})^{1/2}$.

Although a large body of experimental data exists for turbulent flows, no detailed experimental data for both the turbulent flow field and concentration field inside of a liquid-phase, confined planar jet are available for model validation. The objective of the present study is to investigate turbulent mixing in a confined planar jet using both PIV and PLIF. The velocity and concentration fields are analyzed to provide insight into the characteristics of turbulent mixing and to validate the results of CFD models.

Experimental Apparatus and Methodology

Flow facility

The experimental setup is shown in Figures 1 and 2. The flow system is designed to provide a shear flow for Reynolds numbers, based on the hydraulic diameter, in the range 5000–100,000. The measurements are carried out in a Plexiglas® test section (Figure 2) with a rectangular cross section of 60 × 100 mm and an overall length of 1 m. The test section is mounted in an adjustable cage so that it can be moved up and down to

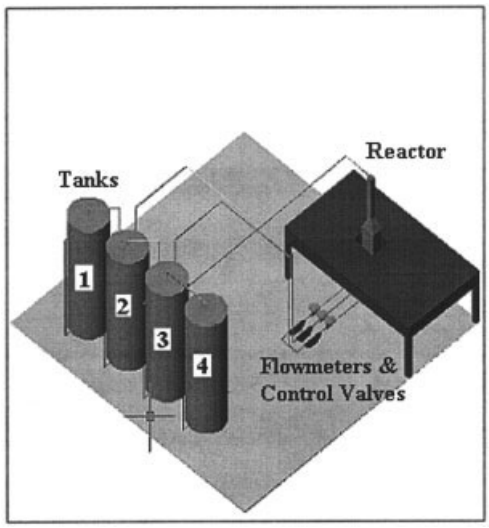

Figure 1. Flow facility used in the PIV and PLIF experiments.

Tanks 1 and 2 are holding tanks; tanks 3 and 4 are receiving tanks.

change the interrogation region without moving the lasers and cameras. The width of each of the three inlet channels is 20 mm. Three feedback control systems (Fieldvue DVC6000, Fisher Controls International Inc., Marshalltown, IA), with flow accuracy of 0.5%, are used to supply constant flow rates to the inlet channels.

Before they enter the test section, uniform flow with reduced free-stream turbulence intensities is produced by flow conditioning with a packed bed of 1-cm spheres, turbulence reducing screens, and 4:1 contractions in two directions. For the present study, the flow rates of the inlet channels were 1.0, 2.0, and 1.0 L/s, respectively; thus the free-stream velocities were 0.5, 1, and 0.5 m/s, respectively. The Reynolds number based on the area-averaged velocity and the hydraulic diameter of the test section was 50,000. The coordinate system in plots presented here is such that x is in the downstream direction and y is in the transverse direction. The flow in the spanwise direction (z) is

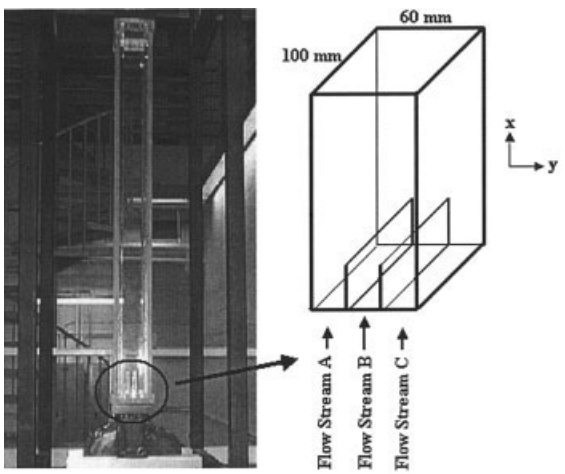

Figure 2. Confined planar-jet test section.

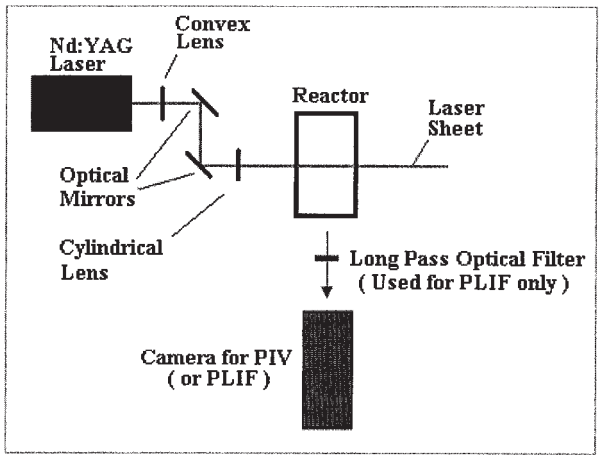

Figure 3. Top view of the optical setup for the PIV and PLIF experiments.

assumed to be nearly homogeneous (except near the front and back walls), and no data were taken in that direction.

Velocity measurements

Particle image velocimetry was used to measure the instantaneous velocity field in a planar cross section of the observed flow. A schematic depicting the PIV (and PLIF) experimental setup is shown in Figure 3. The flow was seeded with hollow glass spheres (Sphericel, Potters Industries Inc., Valley Forge, PA) with a nominal diameter of 11.7 μm and a density of 1.1 g/cm^3. The particles were added to the feed tanks and mixed until they were distributed homogeneously. About 120 g of seed particles were added to the total reservoir volume of 3500 L.

Illumination was provided by a New Wave Research Gemini PIV laser, which is a double-pulsed Nd:YAG laser that emits two independent 532-nm light pulses at a frequency of 15 Hz. The maximum pulse energy is 120 mJ and the pulse duration is about 5 ns. A time delay between the two laser pulses of 600 μs was used in the present study. Using a series of mirror and cylindrical and spherical lenses, the laser beam was formed into a thin light sheet with a thickness of about 0.5 mm passing through the reactor at the centerline of the cross-stream direction. The waist of the light sheet was located near the centerline in the y-direction.

Images of the seeded flow were obtained at a frame rate of 8 images/s using a 12-bit LaVision Flowmaster 3S CCD camera with a resolution of 1280 $\times$ 1024 pixels. The laser and cameras were connected to a host computer that controlled the timing of laser illumination and image acquisition. Two images were captured per realization, and the corresponding velocity field was computed using a cross-correlation technique.[32,33] A multipass interrogation scheme with decreasingly smaller window sizes was used with a final interrogation spot size measuring 16 $\times$ 16 pixels, corresponding to 0.9 mm on a side. With 50% overlap between adjacent interrogation spots, the spatial resolution was 0.45 mm in both the x- and y-directions. The only postprocessing performed on the vector fields was the removal of bad vectors. No smoothing of vector fields was performed. At each observed location, 2500 image pairs were taken and then analyzed.

Using the exit width of the jet as the characteristic length scale, the Kolmogorov scale in the present study was estimated to be about 75 μm, based on Eqs. 1 and 2. The spatial resolution of the PIV measurements is about 6η; therefore, the measurements cannot adequately resolve the smallest scales of the flow. However, because the primary interest in this study is in the determination of the first- and second-order flow statistics such as mean velocity and turbulence intensity, the loss of the fine-scale information should not affect the results.

Uncertainties in the velocity measurements include errors introduced during the recording of the images and bias introduced by large velocity gradients.[34] The maximum uncertainty of the measurements in particle displacement between laser pulses can be estimated as one-tenth of the particle image diameter.[35] The centerline free-stream velocity corresponds to a displacement of 600 μm and the side free-stream velocities correspond to a displacement of 300 μm; thus, the maximum experimental uncertainty is $\pm 1.3\%$ for the center free stream and $\pm 2.7\%$ for the side free streams.

Concentration measurements

A similar optical setup was used for the PLIF measurements, except that the camera was placed closer to the reactor than in the PIV measurements, giving a smaller field of view. Based on the area viewed per pixel, the spatial resolution for PLIF measurements was 0.026 mm. However, the diffraction-limited spot size for the lens was 0.1 mm, which is a better estimate of the PLIF spatial resolution. Rhodamine 6G was used as the passive scalar. In the center stream, the source concentration of Rhodamine 6G was 45 μg/L, whereas the other two streams were pure water. Rhodamine 6G emits broadband fluorescence with a peak emission around 555 nm when excited by light from the Nd:YAG laser.[36] To ensure that reflected or scattered laser light does not interfere with the fluorescence measurements, the camera lens was fitted with a long-pass (that is, low pass for frequency) optical filter that blocked light < 555 nm. The concentration field images were captured at a frame rate of 8 images/s. Because the flow could not be recirculated during PLIF measurements, the number of images that could be collected per run was limited by the volumes of the feed tanks. For the data presented here, 1500 images were taken at each observed location.

Nd:YAG lasers have a Gaussian energy distribution, so it is impossible to obtain a uniform energy distribution throughout the entire light sheet. This drawback can be significant for PLIF that is based on light intensity.[23] Furthermore, the intensity of a laser beam decays as it passes through the dye solution because of absorption. Crimaldi and Koseff[17] claimed that under appropriate experimental conditions, the local intensity of the fluoresced light F is proportional to the local intensity of the excitation source I and to the local concentration of the dye C, so that F is given by

$$F(x, y) = \alpha I(x, y) C(x, y) \tag{6}$$

where α is a constant that can be determined empirically. In the present study, we found that this relationship was valid for dye concentrations up to 100 μg/L with our experimental setup.

To eliminate any variation of the local intensity of the excitation source, we used the following procedure for the calibration of the concentration measurements. A series of 1000 dark images was taken and averaged at each pixel to measure the gray offset value distribution in the interrogation field, and this was used to remove the dark-field component from each PLIF image. Variations in illumination intensity were accounted for by filling up the test section with the source dye solution and recording a series of 200 in situ calibration images at each measurement location. The instantaneous PLIF images at each measurement location were then normalized for illumination variations using the ensemble mean of the calibration images.

Overview of CFD Models

In most applications of CFD models, the Reynolds equations are closed either by turbulent-viscosity models or by Reynolds-stress models. In this work, we adopt a turbulent-viscosity–based model that is widely used in industry, that is, the k–ε model.[37] All the model constants adopt their standard values.[38] The k–ε model is generally regarded as being easy to implement and computationally inexpensive.[22] However, k–ε calculations in the near-wall region can be computationally intensive as a result of two principal difficulties: (1) sharp gradients in k and ε, and (2) source terms becoming very large. To obtain the desired accuracy with reasonable computational cost, a two-layer k–ε model (see Appendix for details) has been implemented in our finite-volume Reynolds-averaged Navier–Stokes (RANS) code.[39,40] The performance of this model is evaluated by comparing predicted single-point turbulence statistics with time-averaged PIV data.

Although turbulent transport of an inert scalar can be successfully described by a small set of statistical moments, the same is not true for reactive scalar fields, which are strongly coupled through the chemical source term.[5] According to how they treat the SGS concentration fluctuations in the closure for the chemical source term, CFD models for liquid-phase turbulent reacting flows can be roughly classified into four general categories: moment methods, conditional moment methods, multienvironment presumed probability density function (PDF) methods and transported PDF methods.[5,41,42] In the moment methods, the SGS fluctuations are represented by a mean-field approximation involving low-order moments. No attempt is made to represent the entire PDF that is present at the mesoscopic level. In general, these models are insufficient for predicting byproduct selectivity in chemical reactors.[43] Conditional moment methods use a presumed PDF model to account for the SGS fluctuations of the mixture fraction. The reaction progress variables are modeled in terms of their mean values conditioned on the value of the mixture fraction. The conditional moments can be found either by a linear interpolation procedure[44] or by solving a transport equation.[45] Multienvironment presumed PDF methods assume that the joint PDF of the SGS fluctuations can be represented by a small number of "environments," each of which is parameterized by its probability and its chemical composition.[5,42,46] In this work, we will validate both a moment model for the mean and variance of an inert scalar and a transported PDF model for the scalar PDF. Although the transported PDF model is not strictly required to describe mixing of inert scalars, it will be needed in our future work with reacting scalars.

Scalar moment transport model

Turbulent mixing encountered in chemical process equipment is almost always inhomogeneous. The most frequently used inert scalar statistics are the scalar mean $\langle\phi\rangle$ and the scalar variance $\langle\phi'^2\rangle$, where ϕ represents an inert scalar and ϕ' its fluctuation. Denoting the Reynolds average velocity and the fluctuation velocity as $\langle \boldsymbol{u}\rangle$ and $\boldsymbol{u}'$, respectively, the transport equations of an inert scalar mean and variance are

$$\frac{\partial\langle\phi\rangle}{\partial t} + \langle u_j\rangle \frac{\partial\langle\phi\rangle}{\partial x_j} = \Gamma\nabla^2\langle\phi\rangle - \frac{\partial\langle u_j'\phi'\rangle}{\partial x_j} \tag{7}$$

and

$$\frac{\partial\langle\phi'^2\rangle}{\partial t} + \langle u_j\rangle \frac{\partial\langle\phi'^2\rangle}{\partial x_j} = \Gamma\nabla^2\langle\phi'^2\rangle - \frac{\partial\langle u_j'\phi'^2\rangle}{\partial x_j} + P_\phi - \varepsilon_\phi \tag{8}$$

where Γ is the molecular diffusivity, and repeated indices imply summation. The scalar-variance production term P_ϕ is defined by

$$P_\phi \equiv -2\langle u_j'\phi\rangle \frac{\partial\langle\phi\rangle}{\partial x_j} \tag{9}$$

Thus, Eqs. 7 and 8 have three unclosed terms: the scalar flux $\langle u_j'\phi'\rangle$, the scalar-variance flux $\langle u_j'\phi'^2\rangle$, and the scalar dissipation rate ε_ϕ, which is defined by

$$\varepsilon_\phi \equiv 2\Gamma\left\langle \frac{\partial\phi'}{\partial x_i}\frac{\partial\phi'}{\partial x_i}\right\rangle \tag{10}$$

To be consistent with the k–ε model used to close the Reynolds stresses, the scalar and scalar-variance fluxes in this study are closed by invoking a gradient-diffusion model,[47] resulting in

$$\langle u_j'\phi'\rangle = -\Gamma_T \frac{\partial\langle\phi\rangle}{\partial x_j} \tag{11}$$

and

$$\langle u_j'\phi'^2\rangle = -\Gamma_T \frac{\partial\langle\phi'^2\rangle}{\partial x_j} \tag{12}$$

with $\Gamma_T = \nu_T/\mathrm{Sc}_T$. ν_T is the eddy viscosity and Sc_T is the turbulent Schmidt number that equals 0.7 in this study unless specified elsewhere. The scalar dissipation rate is related to the turbulent frequency ε/k by the equation[48]

$$\varepsilon_\phi = C_\phi \frac{\varepsilon}{k}\langle\phi'^2\rangle \tag{13}$$

with the empirical constant C_ϕ taken to be 2.0 throughout this work unless specified otherwise. The RANS code solves Eqs. 7 and 8 with closures Eqs. 11–13, the accuracy of which is validated by comparing the simulated scalar mean and variance fields with PLIF data.

Transported PDF model

Transported PDF methods model a transport equation for the joint PDF of the SGS fluctuations of all concentrations.[49] They are the most computationally intensive of the PDF models. However, they offer the distinct advantage that chemical source terms appear in closed form and require no modeling. Therefore, transported PDF methods are powerful methods for treating the complex (finite-rate) chemistry that is often associated with minor species formation. With the development of detailed chemical kinetics based on molecular-level simulations,[50] transported PDF methods are an attractive macroscopic simulation technique for probing turbulence–chemistry interactions. Moreover, transported PDF simulations can be used to validate the assumptions made in simpler closures, and to suggest alternative closures for particular kinetic schemes.[46]

Taking the molecular transport coefficients for all species to be equal, the transport equation of the joint scalar PDF, denoted by f_ϕ, is[49]

$$\frac{\partial f_\phi}{\partial t} + \frac{\partial}{\partial x_j}(\langle u_j\rangle f_\phi) + \frac{\partial}{\partial x_j}[\langle u_j'|\boldsymbol{\psi}\rangle f_\phi] = -\frac{\partial}{\partial\psi_\alpha}[\langle\Gamma\nabla^2\phi_\alpha'|\boldsymbol{\psi}\rangle f_\phi] - \frac{\partial}{\partial\psi_\alpha}\{[\Gamma\nabla^2\phi_\alpha + S_\alpha(\boldsymbol{\psi})]f_\phi\} \tag{14}$$

where $\boldsymbol{\phi}$ and $\boldsymbol{\psi}$ represent the composition vector and the composition field, respectively. $S_\alpha(\boldsymbol{\psi})$ is the chemical source term of species α. $\langle\cdot\,|\,\boldsymbol{\psi}\rangle$ denotes the Reynolds average conditioned on $\boldsymbol{\phi} = \boldsymbol{\psi}$. The scalar-flux term $\langle u_j\,|\,\boldsymbol{\psi}\rangle f_\phi$ can be closed by the gradient-diffusion model as

$$\langle u_j'|\boldsymbol{\psi}\rangle f_\phi = -\Gamma_T \frac{\partial f_\phi}{\partial x_j} \tag{15}$$

The micromixing term $\langle\Gamma\nabla^2\phi_j\,|\,\psi\rangle$ may be represented by a micromixing model. The interaction-by-exchange-with-the-mean (IEM) model is used in this study.[51] For our case, that of an inert scalar, only one composition variable ϕ is needed, and the chemical source term $\langle\cdot\,|\,\boldsymbol{\psi}\rangle$ is null. However, we retain $S_\alpha(\boldsymbol{\psi})$ for future reference.

In our Lagrangian PDF code,[52-54] Eq. 14 is expressed in terms of stochastic differential equations for "notional" particles. The position and composition of a notional particle are given by $\boldsymbol{X}^*$ and $\boldsymbol{\phi}^*$, respectively, and their values are governed by the following equations[5]:

$$d\boldsymbol{X}^* = [\langle\boldsymbol{u}\rangle(\boldsymbol{X}^*, t) + \nabla\Gamma_T(\boldsymbol{X}^*, t)]dt + \sqrt{2\Gamma_T(\boldsymbol{X}^*, t)}\,dW(t) \tag{16}$$

and

$$d\boldsymbol{\phi}^* = \frac{C_\phi\varepsilon}{2k}(\langle\phi\rangle(\boldsymbol{X}^*, t) - \boldsymbol{\phi}^*)dt + \boldsymbol{S}(\boldsymbol{\phi}^*)dt \tag{17}$$

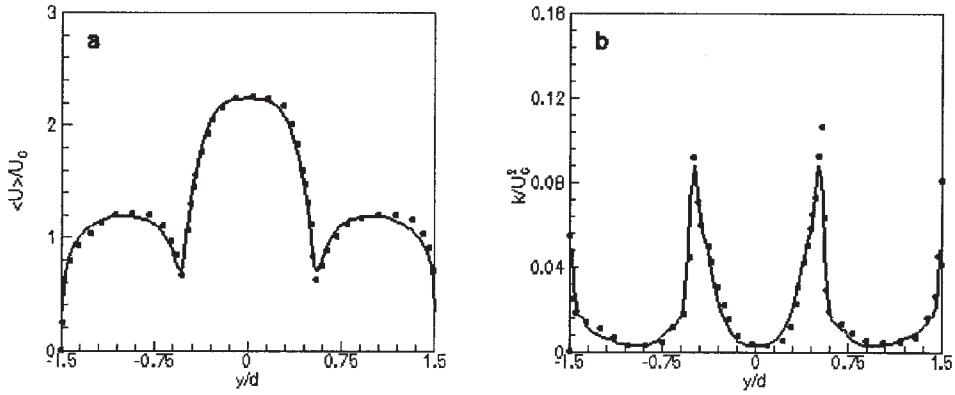

Figure 4. (a) Mean streamwise velocity and (b) turbulent kinetic energy at the entrance plane of the confined planar jet.

—, Simulations; ●, PIV data.

where $dW(t)$ is a multivariate Wiener process, and $\boldsymbol{S}(\boldsymbol{\phi}^*)$ is the chemical source term. $\langle \boldsymbol{u} \rangle(\boldsymbol{X}^*, t)$ and $\langle \boldsymbol{\phi} \rangle(\boldsymbol{X}^*, t)$ are the mean velocity and the estimated scalar mean at the particle location, respectively. The scalar mean and variance are estimated from the compositions of the particles. In the nonreacting flow investigated in this study, $\boldsymbol{S}(\boldsymbol{\phi}^*)$ is null. The turbulence statistics appearing in Eqs. 16 and 17 are taken from the RANS code. Details on the coupling between the flow field and the particle fields in the Lagrangian PDF code can be found elsewhere.[5] The turbulent transport closure defined by Eq. 15 can be validated by agreement of the scalar mean and variance predicted by the PDF code with PLIF data.

Simulation conditions

The performance of the confined planar-jet reactor was simulated using the RANS and PDF models described above. Because no chemical reactions occur, the scalar is inert. The distribution of the experimental data was found to be slightly asymmetric with respect to the centerline because of the jet growing slightly toward one of the walls of the test section. To provide inlet boundary conditions for the simulations, the experimental data of mean velocity and turbulent kinetic energy at the entrance plane of the jet were made symmetric with respect to $y/d = 0$ by averaging and then interpolated linearly between data points. The PIV data for the mean velocity and turbulent kinetic energy at the jet exit and the corresponding inlet boundary conditions for the RANS code are shown in Figure 4. In this study, the PIV data for the turbulent kinetic energy were derived from the streamwise and transverse velocity fluctuations, u' and v', through Eq.18,

$$k = \frac{\langle u'^2 \rangle + 2\langle v'^2 \rangle}{2} \tag{18}$$

More details can be found in the discussion of the CFD predictions for turbulent kinetic energy. The inlet values of dissipation rate were estimated by

$$\varepsilon = A \frac{k^{3/2}}{l_m} \tag{19}$$

where l_m is a characteristic length scale. The length scales l_m were set equal to 0.0035 m for the inner jet and 0.002 m for the outer jets after trial and error investigation that produced a turbulent kinetic energy at $x/d = 0.5$, which agreed with the PIV measurements. Note that these values are smaller than the jet widths, as expected, adopting the value suggested by Antonia et al.[27] By comparing Eqs. 2 and 19, it is known that $l_m/l = (3/2)^{3/2}$ for homogeneous and isotropic turbulence.

Because the flow statistics at the centerline of the channel are only slightly affected by the front and back walls, all simulations were performed on a two-dimensional (2-D) grid by neglecting gradients in the spanwise direction. An 81×121 Cartesian grid was generated for the computational domain. The grid has nonuniform cells with denser grid points near stream interfaces and walls to capture more details associated with sharp gradients. It was chosen after making grid-independency tests to ensure a grid-independent solution. However, its resolution is lower than the spatial resolution in the PIV/PLIF measurements. Thus, the inlet boundary conditions shown in Figure 4 effectively cut off the high gradients measured in the shear layers because of the difference in resolution. This was found to have no impact on the predicted flow statistics. A fixed time step that equals 0.005 s was used in the transported PDF code.

Results and Discussion

A typical velocity field from PIV measurements is shown in Figure 5. To aid in the visualization of turbulent structures, a convective velocity of 0.75 m/s has been subtracted from each vector in this figure. As a reminder, the coordinate system used in Figure 5 is such that the tips of the splitter plates are located at $x = 0$ and $y = \pm 10$, and the centerline between two side walls is along $y = 0$. Similarly, Figure 6 shows an instantaneous concentration field. The contour levels represent mixture fraction, which is the concentration normalized by the concentration of the dye in the inner feed stream C_0. In Figures 7–12, u and v denote the streamwise and transverse velocity components, respectively.

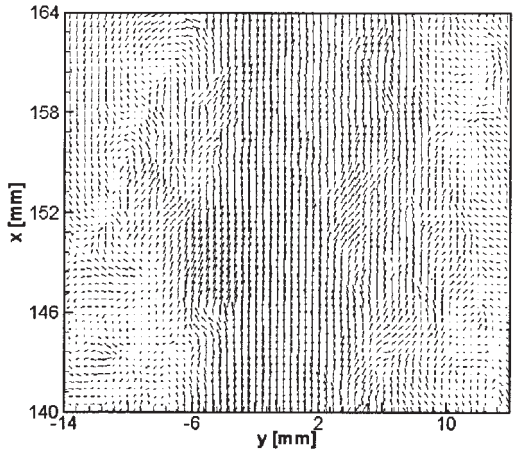

Figure 5. Sample instantaneous velocity field.

Experimentally measured mean velocities and Reynolds stresses

The ensemble averaged streamwise velocity profiles for six representative downstream locations are shown in Figure 7. The mean velocity components are normalized by $U_c = 0.5$ m/s, which is the difference between the inlet free-stream velocities of the center and side streams. The y-axis has been normalized by the inlet jet width, $d = 20$ mm. This normalization of the transverse coordinate is used throughout the presented work. As Figure 7 shows, at the inlet level ($x/d = 0$), the velocity profile is fairly symmetric with two mixing layers growing from the tips of the splitter plates, and this symmetry is maintained in each of the downstream velocity profiles. However, these mixing layers are short lived, and they quickly grow together as the flow convects downstream. Indeed, the potential core in the center jet has completely disappeared at $x/d = 4.5$. As the flow progresses downstream, the potential cores in the outer streams also disappear, and the flow continues its development toward channel flow.

Reynolds stress profiles, normalized by U_c^2, for the same six locations are shown in Figures 8–10. At all six measurement locations, $\langle u'u' \rangle$ (Figure 8) is approximately twice as large as the $\langle v'v' \rangle$ (Figure 9), and both are approximately symmetric about the jet centerline. The stresses are highest just downstream of the tip of the splitter plates, just after the incoming boundary layers have merged to form the initial mixing layers, and the stresses decay as the mixing layers grow. After the two mixing layers have grown together, the peak values remain almost constant, whereas the "valley" between the two peaks fills up. However, the two peaks in the Reynolds stress profiles remain distinct even at the farthest downstream measurement location, $x/d = 15$. Also note that because of the boundary layers developing along the sidewalls of the test section, the values of the Reynolds normal stresses increase as the observation point moves toward the wall.

The Reynolds shear stress, $\langle u'v' \rangle$, shown in Figure 10, is asymmetric around the centerline, positive where the mean flow shear stress is negative, and negative where the mean flow

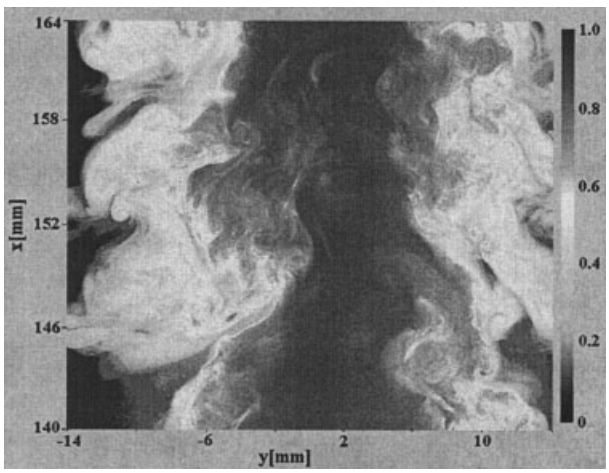

Figure 6. Sample instantaneous concentration field.

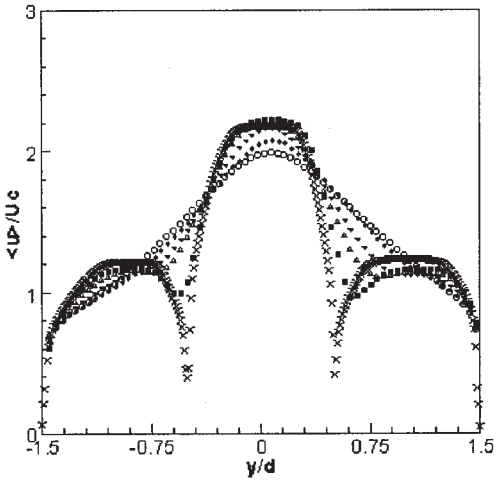

Figure 7. Normalized mean streamwise velocity at various downstream locations as measured by PIV.

×, $x/d = 0$; ■, $x/d = 1$; △, $x/d = 4.5$; ▼, $x/d = 7.5$; ◆, $x/d = 12$; ○, $x/d = 15$.

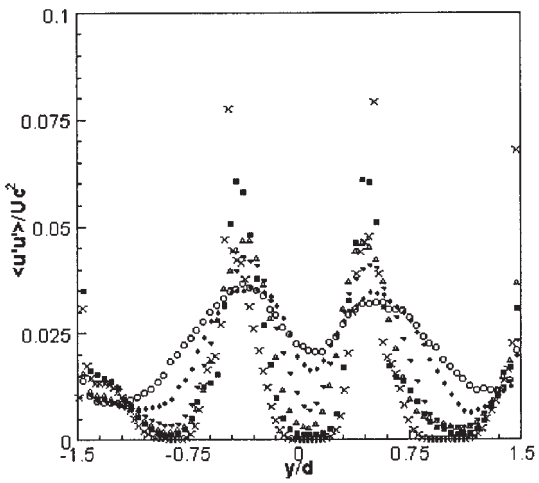

Figure 8. Streamwise Reynolds normal stress at various downstream locations as measured by PIV.

×, $x/d = 0$; ■, $x/d = 1$; △, $x/d = 4.5$; ▼, $x/d = 7.5$; ◆, $x/d = 12$; ○, $x/d = 15$.

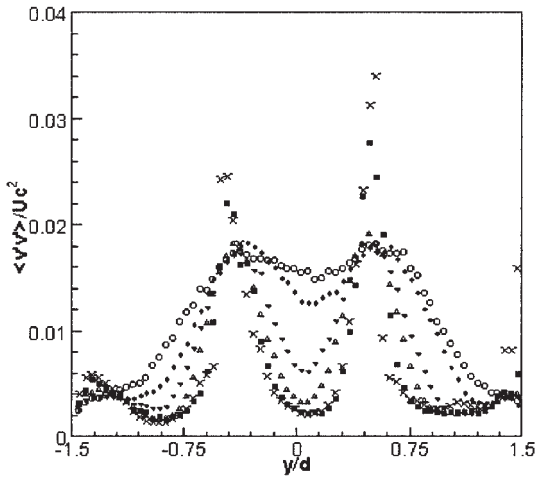

Figure 9. Cross-stream Reynolds normal stress at various downstream locations as measured by PIV.

×, $x/d = 0$; ■, $x/d = 1$; △, $x/d = 4.5$; ▼, $x/d = 7.5$; ◆, $x/d = 12$; ○, $x/d = 15$.

shear stress is positive. Along the centerline of the reactor, which is a plane of symmetry, the Reynolds shear stress is zero. Because of the turbulent boundary layers, the values of shear stress in the regions near walls are nonzero. Moreover, the boundary layers developing along both sides of the splitter plate cause the sign change of Reynolds shear stress in the mixing layers at locations near the tips (such as $x/d = 0$ and $x/d = 1$). The peak Reynolds shear stress is highest just downstream of the splitter plate tips, and decreases with increasing distance downstream.

CFD predictions for mean velocity

The mean streamwise velocity predicted by the RANS code with the two-layer k–ε model is compared with PIV measurements in Figure 11. Comparisons are shown for downstream locations $x/d = 4.5$, 7.5, and 15. The comparisons are good, although the spreading rate of the jet is slightly lower than that measured by PIV, and this characteristic becomes more pronounced as the downstream distance increases. This smaller spreading rate in the RANS calculations is most likely attributable to a lower diffusion rate of the turbulent kinetic energy, as discussed in the next section.

CFD predictions for turbulent kinetic energy

The PIV velocity fields are 2-D measurements, containing only streamwise and transverse velocity components. To obtain the turbulent kinetic energy from the 2-D PIV measurements, the spanwise (that is, out-of-plane) velocity fluctuation must be estimated based on the measured x and y fluctuations. The spanwise fluctuation was assumed to be equal in magnitude to the cross-stream fluctuation (Eq. 18). This assumption is expected to be valid near the inlet because the flow there resembles a pair of mixing layers, and turbulence in mixing layers has this characteristic.[22] Fully developed turbulent channel flow also has this characteristic, so the assumption of comparable transverse and spanwise velocity fluctuations is expected to yield reasonable results. Also recall that PIV measures a filtered velocity field, given that the measurement volume is greater than the Kolmogorov scale. However, because the larger energy containing eddies are fully resolved, errors from the filtered velocity field should not significantly affect the measured turbulent kinetic energy.

Turbulent kinetic energy predicted by the RANS code with a two-layer k–ε model is compared with PIV measurements in Figure 12 for downstream locations $x/d = 1$, 4.5, 7.5, and 15. The RANS code predicts a slightly higher turbulent kinetic energy than that measured by PIV, but in general, the agreement between the two is apparent at all downstream locations.

Experimentally measured scalar mean and scalar variance

Figure 13 shows the transverse profiles of the ensemble-averaged mixture fraction (normalized concentration) across the channel at four downstream locations: $x/d = 1$, 4.5, 7.5, and 15. The mean mixture fraction at $x/d = 1$ is very nearly a top-hat function, with all of the dye located in the center stream. However, as the downstream distance increases, the mean mixture fraction in the center stream decreases and the mean mixture fractions in the outer streams increase because of mass transport of the dye arising from both turbulent mixing and molecular diffusion. As in the mean velocity profiles, the plots are slightly asymmetric because of the jet growing slightly toward one of the walls of the test section.

The mixture-fraction variance is shown in Figure 14. Note that as the mixing layers develop and begin to grow into one another, the peaks of the variance move toward the walls. Also, the experimentally measured peak value of the variance initially increases with increasing distance from the tip of the splitter plate, but after $x/d = 7.5$, it begins to decrease. Because a fully mixed fluid would have a mixture-fraction variance of zero, this behavior after $x/d = 7.5$ is expected. Note also that just as for the Reynolds stresses, two distinct peaks remain in the plots of mixture-fraction variance, even at the farthest downstream measurement location.

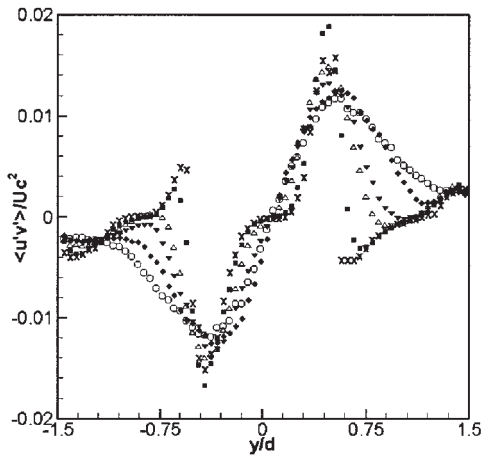

Figure 10. Reynolds shear stress at various downstream locations as measured by PIV.

×, $x/d = 0$; ■, $x/d = 1$; △, $x/d = 4.5$; ▼, $x/d = 7.5$; ◆, $x/d = 12$; ○, $x/d = 15$.

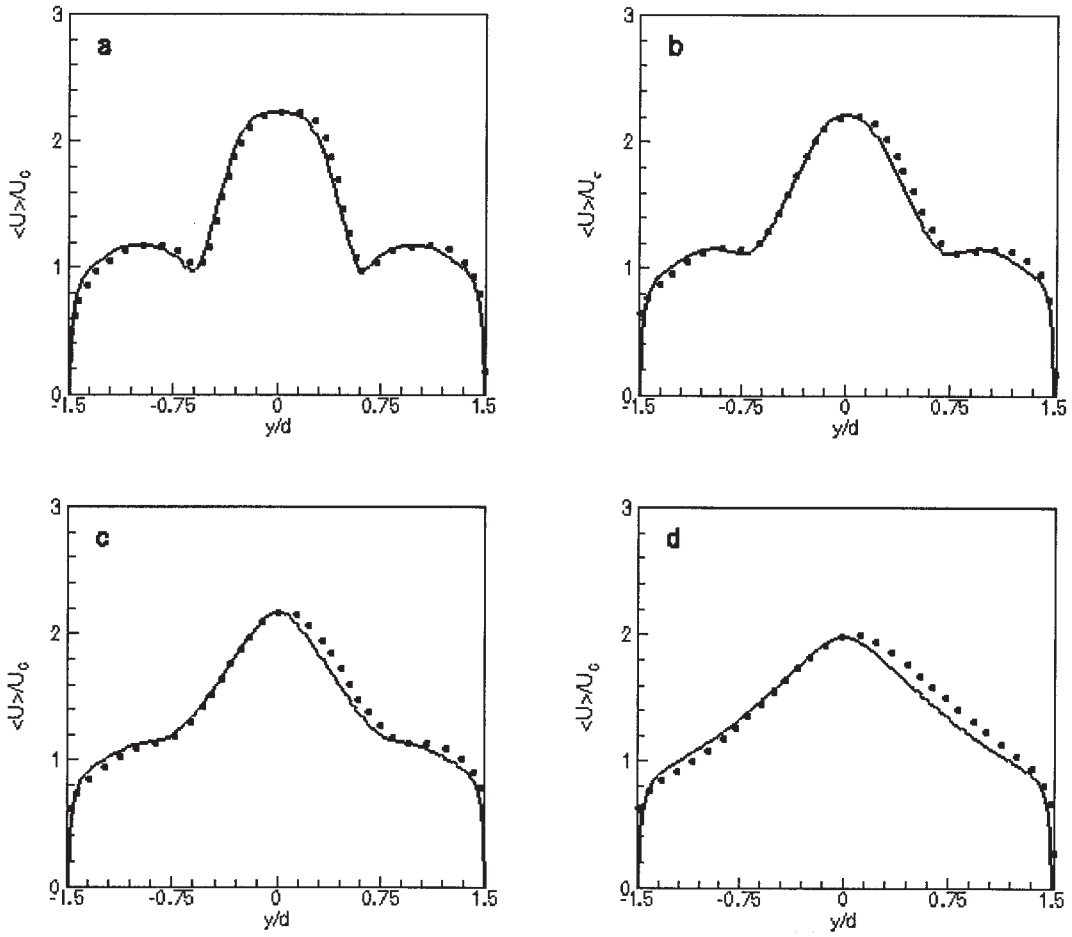

Figure 11. Comparison of the mean streamwise velocity profiles as measured by PIV (symbols) and as calculated from the RANS code (solid line) for (a) $x/d = 1$, (b) $x/d = 4.5$, (c) $x/d = 7.5$, and (d) $x/d = 15$.

CFD predictions for mean mixture fraction

The mean mixture-fraction fields predicted by the RANS and transported PDF codes are compared with the experimental results at various downstream locations in Figure 13, and they agree quite well with the PLIF data. The results indicate that the gradient-diffusion model (Eqs. 11 and 15) accurately predicts the scalar flux for this flow geometry. The lower spreading rate of the mean mixture fraction in the simulations suggests that the turbulent Schmidt number required in Eqs. 11 and 15 is slightly less than the typical value of 0.7. By adopting $Sc_T = 0.5$, the agreement between the CFD simulations and PILF data improves as shown in Figure 13.

CFD predictions for mixture-fraction variance

The profiles of the mixture-fraction variance as predicted by the RANS and the transported PDF codes are compared with experimental data at various downstream locations in Figure 14. The RANS code and the PDF code yield similar results except at $x/d = 1$, where the PDF code predicts a higher variance than the RANS code. In theory, grid-independent solutions for the mean and variance should be exactly the same for both codes. Thus, the higher values observed near the inlet with the PDF code are an indication that a much smaller time step is required in that region where turbulent mixing is slow. In general, both codes predict a higher mixture-fraction variance in the shear layers, where the variance peaks in value, than was measured experimentally. As seen in Figure 14, the agreement cannot be improved by reducing the turbulent Schmidt number to 0.5. Instead, because of the higher turbulent diffusivity, the mixture-fraction variance at each streamwise position reaches a maximum value that is even higher than that given by $Sc_T = 0.7$ at a cross-sectional position that is further from the centerline.

If the scalar dissipation term ε_ϕ is set to zero (this is equivalent to turning off the micromixing model in the PDF code), the analytical solution to Eq. 8 becomes

$$\langle \phi'^2 \rangle = (1 - \langle \phi \rangle)\langle \phi \rangle \tag{20}$$

The numerical simulation results show (Figure 15) that the PDF code and the RANS code accurately predict this analytical solution. Thus, the scalar-variance flux (Eq. 12) was correctly implemented in the RANS code and the grid density at downstream locations was fine enough to ensure that both codes predict consistent results.

Figure 13 shows that the mixture-fraction mean (and thus the production of mixture-fraction variance defined by Eq. 9) is accurately predicted. Therefore, the discrepancies of the model

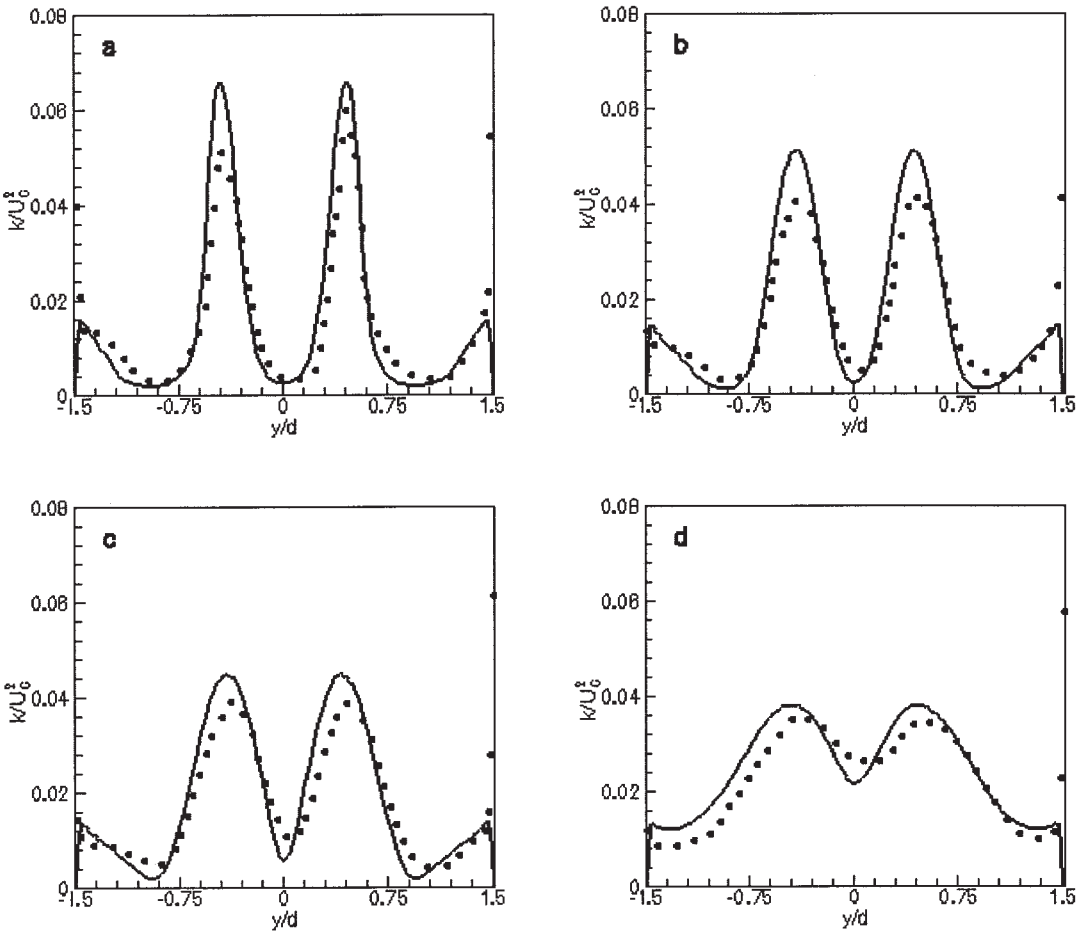

Figure 12. Comparison of the turbulent kinetic energy profiles as measured by PIV (●) and as calculated from the RANS code (—) for (a) $x/d = 1$, (b) $x/d = 4.5$, (c) $x/d = 7.5$, and (d) $x/d = 15$.

predictions and experimental results observed in Figure 14 indicate either inaccuracy in the closure for the scalar dissipation rate (Eq. 13), which is determined by the mixing timescale k/ε, or experimental limitations (stemming from finite resolution of PLIF at high Sc), or both. Near walls, $k \sim O(y^2)$ and $\varepsilon \sim O(1)$ as $y \rightarrow 0$. This results in a very small mixing timescale and thus a scalar dissipation rate that is so large that the mixture-fraction variance is forced to zero in the near-wall regions. Therefore, in the near-wall regions the predicted mixture-fraction variance shows insufficient diffusion. In fact, Eq. 13 is actually a model for the scalar spectral energy transfer rate through the inertial-convective subrange in homogeneous turbulence, and thus cannot be expected to be accurate in the near-wall regions.

For inhomogeneous turbulence, it can be expected that ε_ϕ depends on the degree of turbulent anisotropy and the mean shear rate. Near the reactor entrance ($x/d = 1$), where the turbulence is neither fully developed nor isotropic, this closure cannot represent the entire energy transfer rate from large to small scales. Nevertheless, this closure is valid in fully developed turbulence when the dissipation scales are in spectral equilibrium with the energy-containing scales. With the development of the flow, the performance of the model gradually improves, resulting in better agreement of the predicted variance and PLIF data (Figures 14b and 14c). The insufficient diffusion at near-wall regions is overshadowed by the more uniform scalar concentration indicated by the PLIF data at those downstream locations. At $x/d = 15$, where the nonzero near-wall mixture-fraction variance shown by PLIF data indicates that the scalar concentration is not uniform near walls, the underestimation by the model is significant. Therefore the performance of the model does not improve in the near-wall region at downstream locations (Figure 14d). Further work will be required to improve the closure for the scalar dissipation rate for this region.

Another factor that must be considered is that the PLIF measurements underestimate the scalar variance because the spatial resolution is insufficient to resolve the smallest mixing scales. By definition, the scalar variance can be found directly from the scalar energy spectrum $E_\phi(\kappa, t)$ by integrating over the space of the wavenumber κ:

$$\langle \phi'^2 \rangle = \int_0^\infty E_\phi(\kappa) d\kappa \tag{21}$$

The spatial resolution of the PLIF measurements is limited by the thickness of the laser sheet. The laser-sheet thickness represented by L^* ($L^* = 5 \times 10^{-4}$ m in this study) determines a cutoff wavenumber

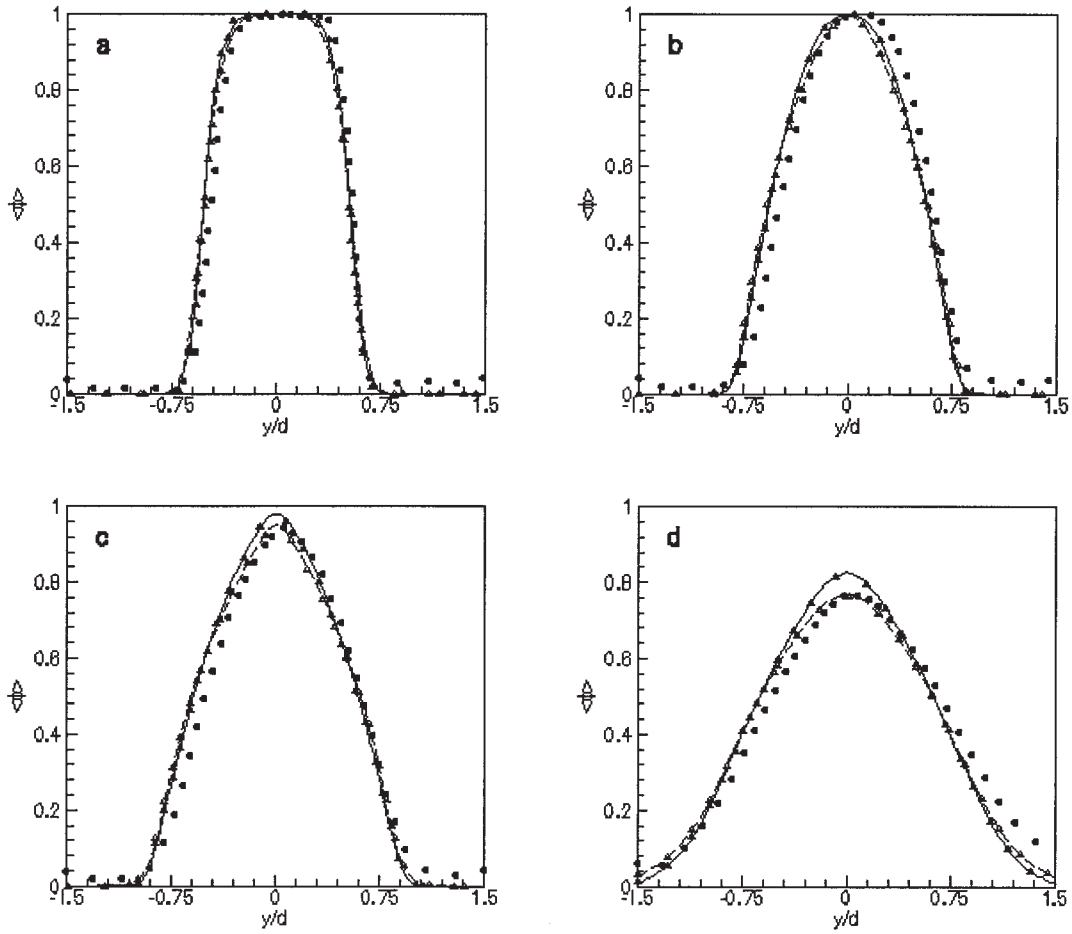

Figure 13. Comparison of mean mixture fraction profiles for (a) $x/d = 1$, (b) $x/d = 4.5$, (c) $x/d = 7.5$, and (d) $x/d = 15$.
●, PLIF; —, RANS, $Sc_T = 0.7$; – – –, RANS, $Sc_T = 0/5$; ▲, PDF, $Sc_T = 0.7$; △, PDF, $Sc_T = 0.5$.

$$\kappa^* = \frac{1}{L^*} \tag{22}$$

Consequently, the scalar variance measured by PLIF decreases to

$$\langle \phi'^2 \rangle^* = \int_0^{\kappa^*} E_\phi(\kappa) d\kappa \tag{23}$$

Using the model scalar spectrum,[5] Table 1 shows the percentage of scalar variance "missed" by the PLIF measurements, defined as $1 - \langle \phi'^2 \rangle^* / \langle \phi'^2 \rangle$, at each downstream location. The missing variance decreases from 12.68% at $x/d = 1$, to about 5.98% at the furthest downstream distance where the Kolmogorov scale of the turbulence is largest, and thus less of the scalar energy spectrum is cut off. This may account for some of the discrepancies between the experimental results and the simulations.

Nevertheless, even after accounting for the PLIF resolution, Figure 14 indicates that the missing mixture-fraction variance is larger than expected. For example, the maximum variance predicted and measured at $x/d = 4.5$ are 0.048 and 0.035, respectively. Thus, the scalar variance missed by the PLIF measurement is 27%, rather than 9.36%, if the exact scalar variance is 0.048. We are therefore motivated to investigate the effect of C_ϕ on the mixture-fraction variance prediction. From direct numerical simulations,[55] it is known that C_ϕ can vary in the range of 2.0–2.5 for inert scalar mixing in stationary turbulence. Moreover, at large Reynolds numbers C_ϕ will approach a Schmidt number–independent limiting value of 2.43,[5] which is the ratio of the Kolmogorov and the Obukhov–Corrsin constants. By taking $C_\phi = 2.5$ the predicted mixture-fraction variance (Figure 16) matches the PLIF data much better at all downstream locations except for $x/d = 1$. This result is quite interesting because it is usually assumed that C_ϕ in liquid-phase flows should be smaller than that in gas-phase flows as a result of the larger Schmidt number effects.[5] Under these flow conditions, however, it appears that the Reynolds number is high enough to render Schmidt number effects negligible.

Dissipation rate

One of the primary advantages of PIV over pointwise velocity measurement techniques is the capability of measuring vorticity and rate-of-strain fields.[56] This enables us to evaluate the dissipation rate in the flow field. However, in 2-D PIV measurements, the out-of-plane component of velocity is not

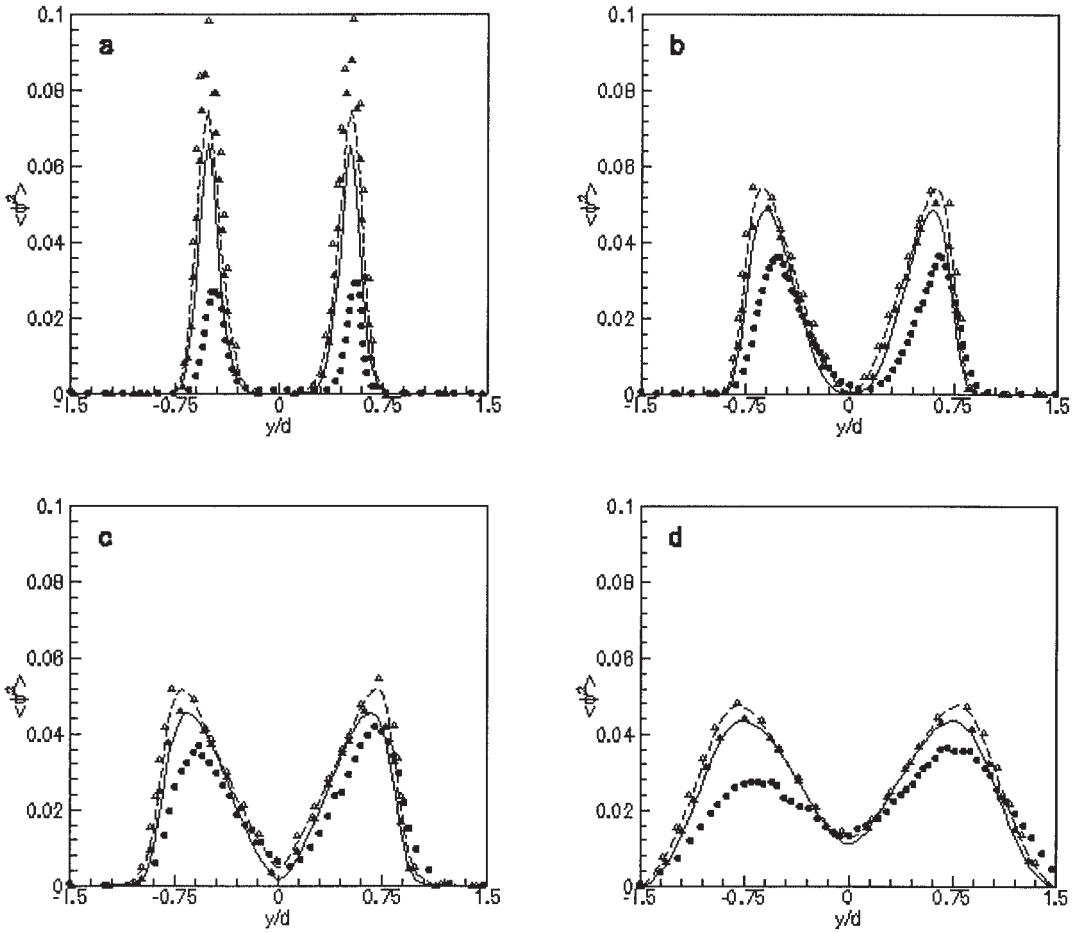

Figure 14. Comparison of mixture fraction variance profiles for (a) $x/d = 1$, (b) $x/d = 4.5$, (c) $x/d = 7.5$, and (d) $x/d = 15$.

●, PLIF; —, RANS, $Sc_T = 0.7$; – – –, RANS, $Sc_T = 0/5$; ▲, PDF, $Sc_T = 0.7$; △, PDF, $Sc_T = 0.5$.

measured. Therefore only four terms of velocity gradient, $\partial\bar{U}/\partial x$, $\partial\bar{U}/\partial y$, $\partial\bar{V}/\partial x$, and $\partial\bar{V}/\partial y$, can be computed directly. Another term, $\partial\bar{W}/\partial z$, may also be determined by using the incompressible continuity equation. Here, $\bar{U}$, $\bar{V}$, and $\bar{W}$ are the x, y, and z components of filtered velocity. Because the other four terms are still missing, some researchers have computed only the so-called 2-D dissipation rate.[25,57] To estimate the turbulence energy dissipation rate using 2-D PIV data, Sharp et al.[58] assumed that the unknown terms were statistically isotropic and thus derivable from the known ones. For a complicated 3-D flow in a stirred vessel, Sheng et al.[30] applied a similar assumption that approximated the dissipation rate by multiplying the sum of the known components of Eq. 3 by a factor of 9/5. In the present study, two methods were used to estimate the dissipation rate: (1) Sheng's method; and (2) assuming $w = v$ and $\partial/\partial z = \partial/\partial y$ to obtain nine terms. Because of the nature of the flow (that is, shear layers and wall-bounded flow), we expect that the second method most closely corresponds to our conditions.

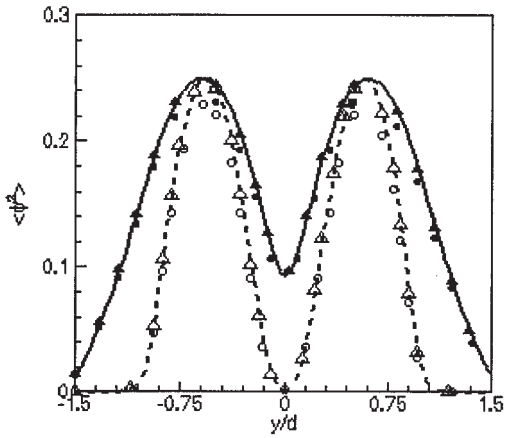

Figure 15. Comparison of analytical solution to scalar variance and calculated scalar variance.

– – –, Analytical solution; ○, RANS; △, PDF at $x/d = 7.5$; —, analytical solution; ●, RANS; ▲, PDF at $x/d = 15$.

Table 1. Estimated Error of PLIF Variance Measurements*

	x/d				
	1	4.5	7.5	12	15
Error (%)	12.68	9.36	8.01	7.75	5.98

*All estimates shown are taken in the left shear layer where the scalar variance reaches its maximum value.

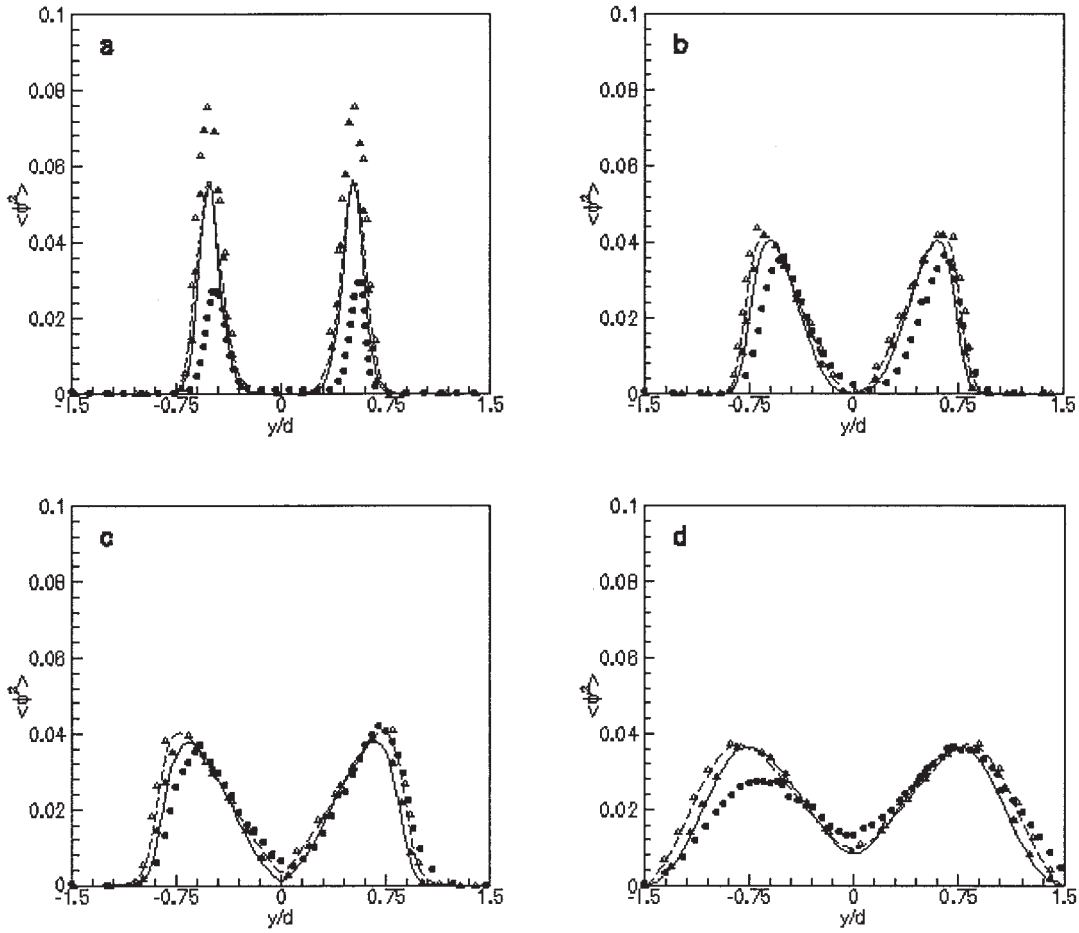

Figure 16. Effect of C_ϕ (C_ϕ = 2.5) on the prediction of mixture fraction variance profiles at (a) x/d = 1, (b) x/d = 4.5, (c) x/d = 7.5, and (d) x/d = 15.

●, PLIF; —, RANS, Sc_T = 0.7; – – –, RANS, Sc_T = 0/5; ▲, PDF, Sc_T = 0.7; △, PDF, Sc_T = 0.5.

The results of the estimations at five downstream locations can be seen in Figure 17. Notice that the dissipation rates calculated using Sheng's method are smaller than those from the second method. However, both methods show that the distribution of the dissipation rate in the reactor is highly inhomogeneous. These graphs also indicate the general trend

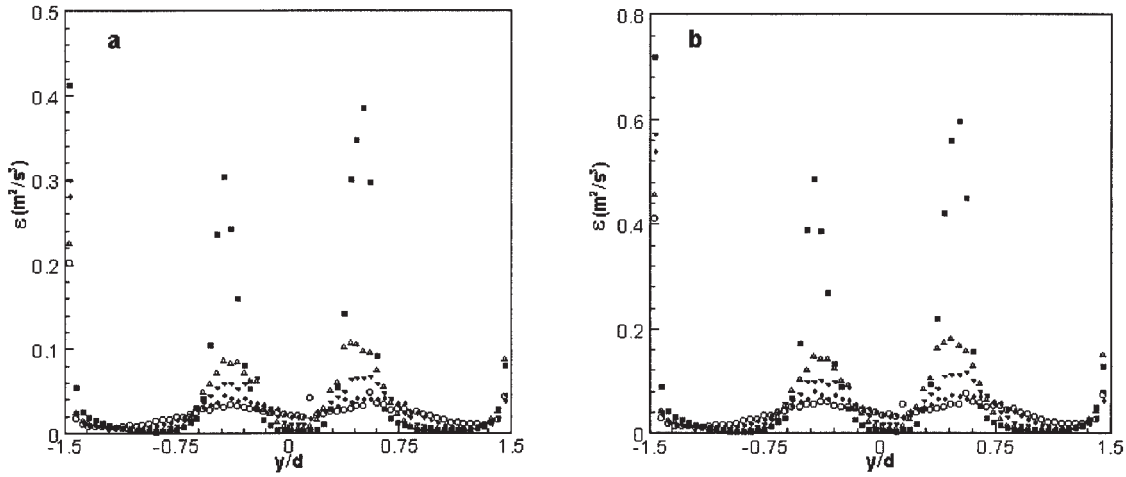

Figure 17. Turbulence dissipation rate at various downstream locations as measured by PIV: (a) estimated by Sheng's method; (b) estimated with nine terms.

■, x/d = 1; △, x/d = 4.5; ▼, x/d = 7.5; ◆, x/d = 12; ○, x/d = 15.

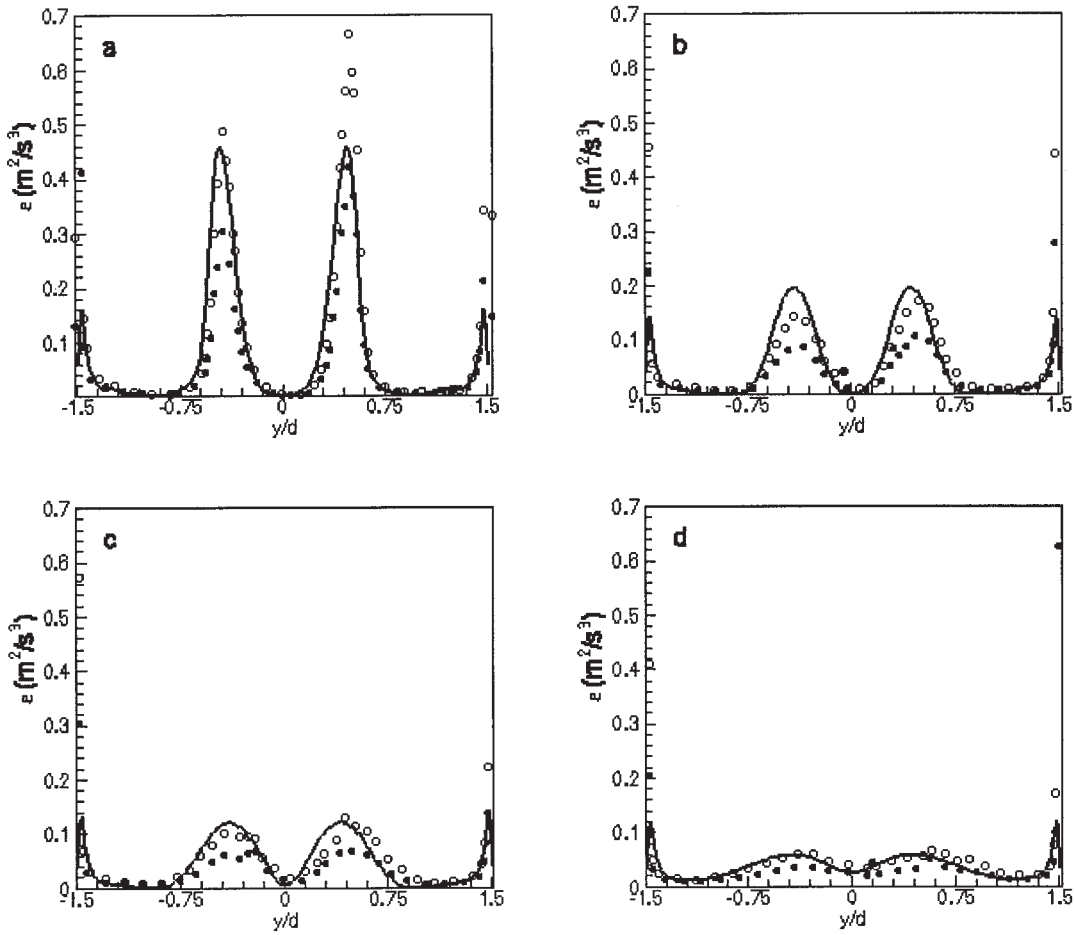

Figure 18. Comparison of dissipation profiles as computed by Sheng's method (●), method 2 (○), and as calculated from the RANS code (—) for (a) $x/d = 1$, (b) $x/d = 4.5$, (c) $x/d = 7.5$, and (d) $x/d = 15$.

that the profile of dissipation rate becomes more uniform in the y-direction as the observation location moves downstream, and the peak values in dissipation decay very quickly at positions nearer the inlet. In comparing with the distributions of energy dissipation rate and turbulent kinetic energy, it is also seen that regions of high values of these quantities coincide, implying a strong correlation between these two properties.

The dissipation rate predicted by the k–ε model is compared with that estimated from PIV measurements in Figure 18. The predicted dissipation rate agrees better with that calculated using nine terms (that is, method 2) than with that found using Sheng's method.

Conclusions

In the present study, velocity and concentration measurements were made for turbulent mixing in a confined planar-jet reactor using PIV and PLIF techniques. The measurements were carried out at six downstream locations with a Reynolds number of 50,000 based on the hydraulic diameter. Statistics of mean velocity, Reynolds stresses, turbulent kinetic energy, mixture-fraction mean, and mixture-fraction variance were calculated. It was observed that two mixing layers grow symmetrically about the centerline of the reactor from the tips of the splitter plates, but these merged together very quickly, and the flow continued its development toward channel flow. It was also noticed that the values of turbulent kinetic energy and Reynolds stress are nonzero in regions near the walls, which indicates that, unlike free jets, the boundary layer developing along sidewalls in the confined jet plays a significant role in the mixing, especially after the potential cores in the outer streams disappear.

The planar velocity data from PIV measurements were also used for estimating the turbulence dissipation rate by computing the Reynolds-averaged SGS dissipation rate. Because the out-of-plane component of velocity fluctuations is unachievable in the present study, some terms of the velocity gradient were not measured. Therefore, two methods were tested to approximate the missing terms using known ones. The results of the dissipation rate from the two methods were compared and showed that the dissipation rate decayed rapidly close to the tips of the splitter plates. It was noted that the distribution of the dissipation rate was symmetric around the centerline and inhomogeneous in the reactor. As expected, the distribution of the dissipation rate also suggested strong correlation with the turbulent kinetic energy.

CFD models were validated against the experiments by comparing computed mean velocity and turbulence fields, and the mixture-fraction mean and variance with PIV/PLIF data.

The Reynolds stresses were closed by a two-layer k–ε model that successfully predicted the turbulent kinetic energy and dissipation rate, with reasonable computational cost even in near-wall regions. The scalar fluxes were closed by gradient-diffusion models. The accurately computed mixture-fraction mean indicates that the scalar flux was well represented by the gradient-diffusion model. The analytical solution to the transport equation of mixture-fraction variance with no dissipation was predicted exactly by both scalar transport models, illustrating that the solutions were grid independent. The scalar dissipation rate was overpredicted by the "equilibrium" closure in near-wall regions, suggesting that this quantity might be better approximated by solving its transport equation. Elsewhere, ε_ϕ was underpredicted by the equilibrium model with $C_\phi = 2$, but well predicted with $C_\phi = 2.5$. In general, the overall agreement between the CFD models and the experimental data is excellent for this rather complex flow.

Acknowledgments

This work was supported by the National Science Foundation through Grants CTS-9985678 and CTS-0336435 and by the Dow Chemical Company.

We extend special thanks to Charles Lipp at Dow Chemical and Ken Junk at Emerson Fisher for their valuable assistance in the design and construction of the flow system, and Albert Harvey at Dow Chemical and Venkatramanan Raman of CTR Stanford for assistance with the CFD codes. We also thank Andrew Gross, Paul Melzer, Marcie Miller, Brian Taylor, and Jon Thortenson, who worked as undergraduate researchers.

Literature Cited

1. Mehta RV, Tarbell JM. An experimental study of the effect of turbulent mixing on the selectivity of competing reactions. *AIChE J.* 1987; 33:1089-1101.
2. Pipino M, Fox RO. Reactive mixing in a tubular jet reactor: A comparison of PDF simulations with experimental data. *Chem Eng Sci.* 1994;49:5229-5341.
3. Baldyga JA, Pohorecki R. Turbulent micromixing in chemical reactors—A review. *Chem Eng J.* 1995;58:183-195.
4. Baldyga JA, Bourne JR. *Turbulent Mixing and Chemical Reactions*. New York, NY: Wiley; 1999.
5. Fox RO. *Computational Models for Turbulent Reacting Flows*. Cambridge, UK: Cambridge Univ. Press; 2003.
6. Ranade VV. *Computational Flow Modeling for Chemical Reactor Engineering*. San Diego, CA: Academic Press; 2002.
7. Jiménez J, Linan A, Rogers MM, Higuera FJ. A priori testing of sub-grid models for chemically reacting non-premixed turbulent shear flows. *J Fluid Mech.* 1997;349:149-171.
8. Vreman B, Geurts B, Kuerten H. Large-eddy simulation of the turbulent mixing layer. *J Fluid Mech.* 1997;339:357-390.
9. Langford JA, Moser RD. Optimal LES formulations for isotropic turbulence. *J Fluid Mech.* 1999;398:321-346.
10. Sohankar A, Davidson L, Norberg C. A dynamic one-equation subgrid model for simulation of flow around a square cylinder. In: Rodi W, Laurence D, eds. *Engineering Turbulence Modelling and Experiments*. Amsterdam: Elsevier; 1999:227-236.
11. Friberg PC, Hjertager BH. Simulation of a 3-dimensional large-scale fermenter with four Rushton turbines. Proc of 2nd Int Symp on Two-Phase Flow Modelling and Experimentation, Pisa, Italy; 1999.
12. Aanen L, Telesca A, Westerweel J. Measurement of turbulent mixing using PIV and LIF. *Mach Graph Vision*. 1999;8:529-543.
13. Fukushima C, Aanen L. Westerweel J. Investigation of the mixing process in an axisymmetric turbulent jet using PIV and LIF. Proc of 10th Int Symp on Application of Laser Techniques to Fluid Mechanics, Lisbon, Portugal; 2000.
14. Meyer KE, Ozcan O, Larsen PS. Point and planar LIF for velocity-concentration correlation in a jet in cross flow. Proc of 10th Int Symp on Application of Laser Techniques to Fluid Mechanics, Lisbon, Portugal; 2000.
15. Kawaguchi Y, Segawa T, Feng Z, Li P. Experimental study on drag-reducing channel flow with surfactant additives—Spatial structures of turbulence investigated by PIV system. *Int J Heat Fluid Flow.* 2002;23:700-709.
16. Olsen MG, Dutton JC. Stochastic estimation of large structures in an incompressible mixing layer. *AIAA J.* 2002;40:2431-2438.
17. Crimaldi JP, Koseff JR. High-resolution measurements of the spatial and temporal scalar structure of a turbulent plume. *Exp Fluids*. 2001; 31:90-102.
18. Kolmogorov AN. The local structure of turbulence in incompressible viscous fluid for very large Reynolds numbers. *Dokl Akad Nauk SSSR*. 1941;30:299-303.
19. Brown GL, Roshko A. On density effects and large structure in turbulent mixing region. *J Fluid Mech.* 1974;64:2775-2814.
20. Mankbadi RR. Dynamics and control of coherent structure in turbulent jets. *Appl Mech Rev.* 1992;45:219-247.
21. Lesieur M, Comte P, Métais O. Numerical simulation of coherent vortices in turbulence. *Appl Mech Rev.* 1995;48:121-147.
22. Pope SB. *Turbulent Flow*. Cambridge, UK: Cambridge Univ. Press; 2000.
23. Law AW, Wang H. Measurement of mixing processes with combined digital particle image velocimetry and planar laser induced fluorescence. *Exp Therm Fluid Sci.* 2000;22:213-229.
24. Tennekes H, Lumley JL. *A First Course in Turbulence*. Cambridge, MA: MIT Press; 1972.
25. Tsurikov MS, Clemens NT. The structure of dissipative scales in axisymmetric turbulent gas-phase jets. AIAA paper 2002-0164. Proc of 40th Aerospace Sciences Meeting, Reno, NV; 2002.
26. Batchelor GK. *The Theory of Homogeneous Turbulence*. Cambridge, UK: Cambridge Univ. Press; 1953.
27. Antonia RA, Satyaprakash BR, Hussain AKMF. Measurements of dissipation rate and some other characteristics of turbulent plane and circular jets. *Phys Fluids.* 1980;23:695-700.
28. Browne L, Antonia A, Shah D. Turbulent energy dissipation in a wake. *J. Fluid Mech.* 1987;179:307-326.
29. Elsener JW, Elsner W. On the measurement of turbulence energy dissipation. *Meas Sci Technol.* 1996;7:1334-1348.
30. Sheng J, Meng H, Fox RO. A large eddy PIV method for turbulence dissipation rate estimation. *Chem Eng Sci.* 2000;55:4423-4434.
31. Smagorinsky J. General circulation experiments with the primitive equation. I. The basic experiment. *Mon Weather Rev.* 1963;91:99-164.
32. Westerweel J. *Digital Particle Image Velocimetry: Theory and Application*. Uitgave, Delft, The Netherlands: Delft Univ. Press; 1993.
33. Kompenhans J, Raffel M, Willert C. *Particle Image Velocimetry—A Practical Guide*. Berlin: Springer-Verlag; 1998.
34. Keane RD, Adrian RJ. Theory of cross-correlation analysis of PIV images. *Appl Sci Res.* 1992;49:191-215.
35. Prasad AK, Adrian RJ, Landreth CC, Offutt PW. Effect of resolution on the speed and accuracy of particle image velocimetry interrogation. *Exp Fluids.* 1992;13:105-116.
36. Penzkofer A, Leupacher W. Fluorescence behavior of highly concentrated Rhodamine 6G solutions. *J Lumin.* 1987;37:61-72.
37. Jones WP, Launder BE. The prediction of laminarization with a two-equation model of turbulence. *Int J Heat Mass Transfer.* 1972; 15:301-314.
38. Launder BE, Sharma BI. Application of the energy-dissipation model of turbulence to the calculation of flow near a spinning disc. *Lett Heat Mass Transfer.* 1974;1:131-138.
39. Wilcox DC. *Turbulence Modelling for CFD*. 2nd Edition. La Cañada, CA: DCW Industries Inc.; 1998.
40. Harvey AD. Generalized turbulent reacting flow code: 1. Equations and numerics. LAD 2003-008. Midland, MI: The Dow Chemical Company Hydrocarbons Research; 2003.
41. Fox RO. Computational methods for turbulent reacting flows in the chemical process industry. *Rev Inst Français Pétrol.* 1996;51:215-243.
42. Fox RO. On the relationship between Lagrangian micromixing models and computational fluid dynamics. *Chem Eng Prog.* 1998;37:521-535.
43. Chakrabarti M, Kerr RM, Hill JC. First order closure theories for a series-parallel reaction air in a simulated homogeneous turbulence. *AIChE J.* 1997;43:902-912.
44. Baldyga J. A closure model for homogeneous chemical reactions. *Chem Eng Sci.* 1994;49:1985-2003.
45. Bilger RW. Conditional moment closure for turbulent reacting flow. *Phys Fluids A.* 1993;5:436-444.

46. Wang LG, Fox RO. Comparison of micromixing models for CFD simulation of nanoparticle formation. *AIChE J.* 2004;50:2217-2232.
47. Taylor GI. Diffusion by continuous movements. *Proc Lond Math Soc*. 1921;20:196-212.
48. Spalding DB. Concentration fluctuations in a round turbulent free jet. *Chem Eng Sci.* 1971;26:95-107.
49. Pope SB. PDF methods for turbulent reactive flows. *Prog Energy Combust Sci.* 1985;11:119-192.
50. Tirtowidjo M. Fundamental kinetic modelling of industrial reactors. Paper 78b. AIChE Annual Meeting, Los Angeles, CA; 1997.
51. Villermaux J, Devillon JC. Représentation de la coalescence et de la redispersion des domains de segregation dans un fluide par un modèle d'Interaction Phénoménologique. *Proceedings of the 2nd International Symposium on Chemical Reaction Engineering*. New York, NY: Elsevier, 1972:1-13.
52. Raman V, Fox RO, Harvey AD, West DH. CFD analysis of premixed methane chlorination reactors with detailed chemistry. *Ind Eng Chem Res.* 2001;40:5170-5176.
53. Raman V, Fox RO, Harvey AD, West DH. Effect of feed-stream configuration on gas-phase chlorination reactor performance. *Ind Eng Chem Res.* 2003;42:2544-2557.
54. Raman V, Fox RO, Harvey AD. Hybrid finite-volume/transported PDF simulations of a partially premixed methane-air flame. *Combust Flame.* 2004;136:327-350.
55. Yeung PK, Xu S, Sreenivasan KR. Schmidt number effects on turbulent transport with uniform mean scalar gradient. *Phys Fluids.* 2002; 14:4178-4191.
56. Adrian RJ. Particle-imaging techniques for experimental fluid mechanics. *Annu Rev Fluid Mech.* 1991;23:261-304.
57. Saarenrinne P, Piirto M. Turbulent kinetic energy dissipation rate estimation from PIV velocity vector fields. *Exp Fluids.* 2000;Suppl: s300-s307.
58. Sharp KV, Kim KC, Adrian RJ. Dissipation estimation around a Rushton turbine using particle image velocimetry. Proc of the 9th Int Symp on Application of Laser Techniques to Fluid Mechanics, Lisbon, Portugal; 1998.
59. Patel VC, Rodi W, Scheuerer G. Turbulence models for near-wall and low Reynolds number flows: A review. *AIAA J.* 1985;23:1308-1319.
60. Shih TH, Mansour NN. Modelling of near-wall turbulence. In: Rodi W, Gani ć EN, eds. *Engineering Turbulence Modelling and Experiments*. Amsterdam: Elsevier; 1990.
61. Rodi W, Mansour NN. Low Reynolds number k–ε modelling with the aid of direct simulation data. *J Fluid Mech.* 1993;250:509-529.
62. Chen HC, Patel VC. Near-wall turbulence models for complex flows including separation. *AIAA J.* 1988;26:641-648.
63. Wolfshtein M. The velocity and temperature distribution in one-dimensional flow with turbulence augmentation and pressure gradient. *Int J Heat Mass Transfer.* 1969;12:301-318.

Appendix

A two-layer near-wall turbulence model

The successful implementation of turbulence models requires the appropriate treatment of the solid boundaries. The standard k–ε model is restricted to high Reynolds number applications. In near-wall regions where effects of low Reynolds number are significant, it fails to predict a satisfactory value of the additive constant in the law of the wall.[39] This difficulty can be overcome by using the popular wall-function method based on the log-law relations. An alternative approach is the low Reynolds number k–ε models that contain damping functions. More details can be found elsewhere.[39,59-61]

The wall-function method is not satisfactory when the law of the wall assumption is questionable, such as in separated flows and in 3-D flows. On the other hand, low Reynolds number k–ε models are not able to accurately predict the flow close to a solid wall even in the relatively simple case of 2-D flows.[62] For this reason, Chen and Patel[62] proposed a two-layer, near-wall turbulence model that is more accurate and computationally efficient. They defined a turbulence Reynolds number as

$$\mathrm{Re}_y = \frac{k^{1/2} y}{\nu} \tag{A1}$$

where y is the distance from the nearest wall and ν is the molecular kinematic viscosity, and divided the domain into two regions: the fully turbulent region (I) where $\mathrm{Re}_y \geq 200$ and the viscosity-affected near-wall region (II) where $\mathrm{Re}_y < 200$. In region I, the standard k–ε model is used. In region II, the one-equation model of Wolfshtein[63] is used to account for the wall proximity effects. The one-equation model requires the solution of only the turbulent kinetic energy in region II. The rate of energy dissipation in this region is specified by

$$\varepsilon = \frac{k^{3/2}}{l_\varepsilon} \tag{A2}$$

where the length scale is given by the expression

$$l_\varepsilon = C_l y[1 - \exp(-\mathrm{Re}_y/A_\varepsilon)] \tag{A3}$$

The eddy viscosity is obtained from the equation

$$\nu_T = C_\mu k^{1/2} l_\mu \tag{A4}$$

where

$$l_\mu = C_l y[1 - \exp(-\mathrm{Re}_y/A_\mu)] \tag{A5}$$

The constants in the length-scale formulas are

$$C_l = KC_\mu^{-3/4} \qquad A_\mu = 70 \qquad A_\varepsilon = 2C_l \tag{A6}$$

where the von Kármán constant K is 0.41. The turbulence Reynolds number depends only on the local turbulence intensity. It does not vanish at separation and remains well defined in regions of flow reversal. Therefore this two-layer approach is applicable in complex flows, and we have incorporated it into our RANS code.

Manuscript received Oct. 6, 2004, and revision received Feb. 14, 2005.